

# Effects of Temporal Discretization on Turbulence Statistics and Spectra in Numerically Simulated Convective Boundary Layers

Jeremy A. Gibbs · Evgeni Fedorovich

Received: 8 November 2013 / Accepted: 19 May 2014 / Published online: 20 June 2014  
© Springer Science+Business Media Dordrecht 2014

**Abstract** Six state-of-the-art large-eddy simulation codes were compared in Fedorovich et al. (Preprints, 16th American Meteorological Society Symposium on Boundary Layers and Turbulence, 2004b) for three airflow configurations in order to better understand the effect of wind shear on entrainment dynamics in the convective boundary layer CBL). One such code was the University of Oklahoma large-eddy simulation (LES) code, which at the time employed a second-order leapfrog time-advancement scheme with the Asselin filter. In subsequent years, the code has been updated to use a third-order Runge–Kutta (RK3) time-advancement scheme. This study investigates what effect the upgrade from the leapfrog scheme to RK3 scheme has on turbulence statistics in the CBL differently affected by mean wind shear, also in relation to predictions by other LES codes that participated in the considered comparison exercise. In addition, the effect of changing the Courant number within the RK3 scheme is investigated by invoking the turbulence spectral analysis. Results indicate that low-order flow statistics obtained with the RK3 scheme generally match their counterparts from simulations with the leapfrog scheme rather closely. CBL growth rates due to entrainment in the shear-free case were also similar using both timestepping schemes. It was found, however, that care should be given to the choice of the Courant number value when running LES with the RK3 scheme in the sheared CBL setting. The advantages of the largest possible (based on the stability criterion) Courant number were negated by degrading the energy distribution across the turbulence spectrum. While mean profiles and low-order turbulence statistics were largely unaffected, the entrainment rate was over-predicted compared to that reported in the original code-comparison study.

**Keywords** Convective boundary layer · Entrainment · Large-eddy simulation · Wind shear

---

J. A. Gibbs (✉) · E. Fedorovich

School of Meteorology, University of Oklahoma, 120 David L. Boren Blvd., Suite 5900,  
Norman, OK 73072, USA  
e-mail: gibbz@ou.edu

## 1 Introduction

The effect of wind shear on the entrainment processes in the atmospheric convective boundary layer (CBL) was investigated in [Fedorovich et al. \(2004b\)](#) (hereafter FEA04). In that study, results from six state-of-the-art numerical codes employing large-eddy simulation (LES) technique were evaluated against each other with a goal to better understand features of the entrainment dynamics that control the growth of the CBL. In order to facilitate the comparison, various turbulence statistics generated by each code were compared for three CBL wind-shear configurations (no shear, imposed height-constant geostrophic wind, and imposed geostrophic wind linearly varying with height). Despite differences in model numerics, all participated codes were found to consistently reproduce mean features of CBL temperature and velocity fields. Differences of CBL turbulence statistics were found to be only slightly dependent on the wind-shear type and increasing with the order of statistics. Specifically, the participated codes demonstrated a considerable scatter in predictions of the third-order moments of the vertical velocity and potential temperature fluctuations. Certain differences were also observed in predictions of the CBL growth with time. Those differences were attributed, in part, to excessive damping of small-scale turbulent fluctuations of velocity in some of the evaluated codes.

One of the LES codes that participated in the FEA04 comparison exercise was the University of Oklahoma LES (OU-LES) code. The core of the OU-LES code is derived from the Delft University LES ([Nieuwstadt 1990](#)) from which several other currently employed atmospheric LES codes also stem. The ability of the OU-LES code to adequately reproduce sheared CBL flows was demonstrated in [Fedorovich et al. \(2001\)](#). Relevance of the OU-LES code was further confirmed in [Fedorovich et al. \(2004a\)](#) through comparative studies of the shear-free CBL in conjunction with re-evaluated bulk models and water-tank data. The OU-LES code numerically solves the filtered Navier-Stokes equations of motion and scalar transport equations in the Boussinesq approximation, with advection/convection terms in the equations being approximated using second-order, centred finite differences. The subgrid turbulence kinetic energy (STKE) closure implemented in the code is designed after Deardorff (1980). At the time of the study reported in FEA04, the prognostic equations were integrated in time using the leapfrog scheme, which is centred and second-order accurate in time. The [Asselin \(1972\)](#) filter was employed within the leapfrog scheme in order to prevent time splitting of the solution and to damp artificial modes. The filter effectively reduced the leapfrog-scheme accuracy to the first order, which made the numerical solution more diffusive and enhanced damping of large wavenumber turbulent fluctuations. Various changes were made in subsequent years to modernize the code. One of the major upgrades was the implementation of the third-order Runge–Kutta (RK3) time-integration scheme using the version described in [Sullivan et al. \(1996\)](#).

Numerical stability of a given timestepping scheme is commonly described in terms of the so-called Courant number, which is a measure of how far a generic wave-like disturbance traverses the numerical domain over one integration timestep relative to the numerical grid spacing ([Durran 2010](#)). Since instability is manifested through the error growth in time, a timestep scheme would be unstable wherever the wave amplification factor becomes  $>1$ . By considering the amplification factor as a function of the wavenumber and Courant number one can determine the maximum Courant number value for which the system is stable for all wavenumbers present in the solution. For the leapfrog scheme with Asselin filter employed in the old version of the OU-LES code ([Fedorovich et al. 2001](#)), the maximum stable Courant number is 0.75 in the case when the leapfrog scheme is used together with the centred second-order spatial differentiation. In the case of the RK3 scheme used in combination with spatial

differentiation of the second order, the maximum Courant number value that provides for the stable solution is 1.73 (Durran 2010). The corresponding increase in the time-integration efficiency is one of the principal assets of the RK3 scheme. Details regarding the leapfrog and RK3 stability properties are presented in Sect. 2.2.

Our present study examines how CBL turbulent flow statistics considered in FEA04 are affected by the upgrade of the time integration scheme. The effects of the changing Courant number in the RK3 scheme are studied as well. The three CBL flow configurations analyzed in FEA04, one without wind shear and two with differently imposed wind shears, were simulated using the modernized version of the OU-LES code. This version of the code uses an adaptive timestep based on a prescribed Courant number restriction. Each CBL case was run with three different Courant numbers in order to better understand the effects of numerical diffusion on simulated flow statistics. Spectral characteristics of simulated CBL flow fields were also investigated in order to obtain insights into the influence of numerics on the turbulence scale structure. Mean vertical profiles of simulated temperature and velocity (not shown), along with various turbulence statistics, were compared with those considered in FEA04. In addition to the profiles of flow statistics obtained at a given time by averaging over horizontal planes (as was done in FEA04), the 30-min averaged profiles were obtained and analyzed in order to examine how such averaging affects the steadiness of turbulence statistics of different orders.

Description of simulation set-ups, the numerical properties of the leapfrog and RK3 schemes, and the evaluated flow statistics are presented in Sect. 2. Comparisons of the simulated flow statistics with their counterparts from FEA04 are conducted in Sect. 3. Results are discussed in Sect. 4, and conclusions are given in Sect. 5.

## 2 Experimental Design

### 2.1 Simulation Set-Up

Following the experimental set-up described in FEA04, simulations were conducted on a  $256 \times 256 \times 100$  numerical grid with a uniform horizontal spacing of  $\Delta x = \Delta y = 40$  m and a uniform vertical spacing of  $\Delta z = 20$  m. Lateral boundary conditions for prognostic flow variables (resolved velocity components and scalars) and the pressure perturbation (i.e. from the geostrophic pressure gradient) were periodic. The top boundary incorporated a sponge layer in the upper 20 % of the domain. The surface virtual temperature flux was set equal to  $0.1 \text{ Km s}^{-1}$  and held constant in time. Monin–Obukhov similarity relationships were applied at the lower boundary locally to relate dynamic and thermal properties of the flow in the near-surface region. As indicated in Sect. 1, a CBL with three different wind-shear configurations was investigated: (i) CBL with no mean shear (NS), (ii) CBL with height-constant geostrophic wind of  $20 \text{ ms}^{-1}$  (GC), and (iii) CBL with linearly increasing geostrophic wind from zero at the surface to  $20 \text{ ms}^{-1}$  at the top of the simulation domain (GS). In both CBL cases with shear, the  $y$  component of the geostrophic wind was set to zero. Initially, the virtual potential temperature increased with height at a uniform rate of  $0.003 \text{ km}^{-1}$ .

As illustrated in Fig. 1, the extent of numerical damping, represented by the amplification factor values  $< 1$ , varies across spatial scales (wavenumbers) and Courant number values. In order to evaluate effects of the changing Courant number  $C$ , simulations for each CBL case were run with  $C$  set to its maximum stable value ( $C_{\max}$ ), one-half of its maximum stable value ( $C_{\max}/2$ ), and one-fourth of its maximum stable value ( $C_{\max}/4$ ). Hereafter, these LES runs with different Courant number values are referred to as **C1**, **C2**, and **C4**, respectively.

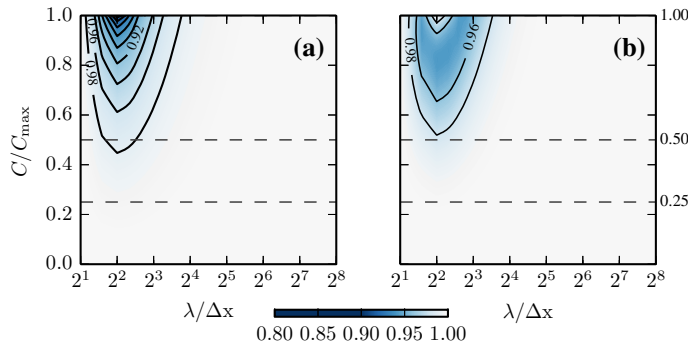


**Fig. 1** Normalized amplification factor for the leapfrog (panel **a**) and RK3 (panel **b**) time-integration schemes. Here,  $C = c\Delta t/\Delta x$  is the Courant number,  $c$  is the advection velocity,  $\Delta t$  is model timestep,  $\Delta x$  is grid spacing,  $\lambda$  is wavelength, and  $C_{\max}$  is the maximum stable Courant number for the employed advection/time-integration setup

## 2.2 Stability Properties of the Employed Time-Integration Scheme

In the OU-LES code, advection/convection terms are discretized using a second-order, centred, finite-difference scheme. For one-dimensional advection, the corresponding advection operator may be written as

$$f(\phi_j^n) = -c \frac{\phi_{j+1}^n - \phi_{j-1}^n}{2\Delta x}, \quad (1)$$

where superscripts indicate time levels, subscripts refer to the spatial location,  $\phi$  is the advected quantity,  $c$  is the advection velocity, and  $\Delta x$  is grid spacing (Durran 2010). The centred, second-order accurate leapfrog scheme advances the system in time according to

$$\phi_j^{n+1} = \widetilde{\phi_j^{n-1}} + 2\Delta t f(\phi_j^n), \quad (2)$$

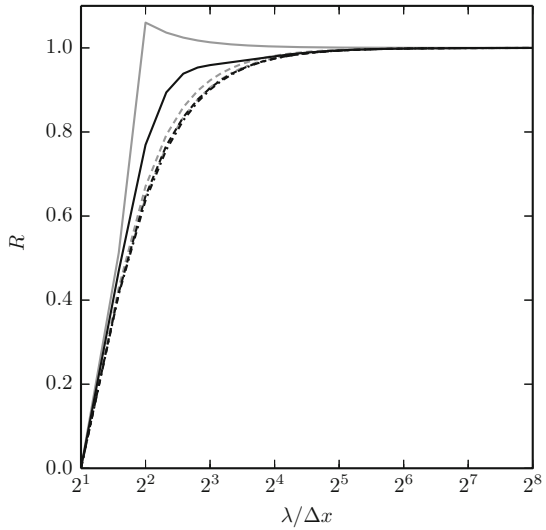
where the tilde represents filtered quantities (Durran 2010). The Asselin (1972) filter, used to stabilize the solution, is applied as

$$\widetilde{\phi_j^n} = \phi_j^n + \epsilon \left( \phi_j^{n+1} - 2\phi_j^n + \widetilde{\phi_j^{n-1}} \right), \quad (3)$$

where  $\epsilon = 0.25$  is the most commonly used Asselin-filter constant. The so-called von Neumann stability analysis (Durran 2010) allows us to investigate the stability of the advection/time-integration scheme. The amplification factor  $A(k) = a(k)^{n+1}/a(k)^n$  represents the growth of a wave over a single timestep as it passes through the system, where  $k$  is wavenumber and  $a(k)^p$  is the amplitude of a discrete Fourier mode at time level  $p$ . The system is deemed stable if  $|A(k)| \leq 1 \forall k$ . The maximum Courant number for this system that satisfies the stability criteria is  $C_{\max} = 1 - \epsilon = 0.75$  (Shapiro and Fedorovich 2008).

The modulus of the amplification factor for the leapfrog scheme is shown in Fig. 1 as a function of the normalized Courant number ( $C/C_{\max}$ ) and normalized wavelength ( $\lambda/\Delta x$ ). Here, we only consider the region where the stability criterion is satisfied ( $C/C_{\max} \leq 1$ ). It is visually apparent that damping extends from waves of size  $2\Delta x$  to  $14\Delta x$ , with the maximum occurring at  $4\Delta x$ . It is also evident that damping decreases with decreasing Courant number, and extends to approximately  $0.45C_{\max}$ .

**Fig. 2** Relative phase ratio for the leapfrog (grey lines) and RK3 (black lines) time-integration schemes. Here,  $R = c_d/c_a$  is the ratio of phase speeds for the wave passing through the discretization scheme and the analytical wave, respectively. Solid lines correspond to **C1** case, dashed lines to **C2** case, and dashed-dotted lines to **C4** case



On the other hand, the finite-difference expression (1) may also be passed through the RK3 time-integration scheme (Sullivan et al. 1996),

$$\phi_j^* = \phi_j^n + \frac{1}{3} \Delta t f(\phi_j^n), \quad (4a)$$

$$\phi_j^{**} = \phi_j^n + \frac{1}{2} \Delta t f(\phi_j^*), \quad (4b)$$

$$\phi_j^{n+1} = \phi_j^n + \Delta t f(\phi_j^{**}). \quad (4c)$$

where the (\*) superscript represents an intermediate level between timesteps. It has been shown that the maximum stable Courant number for this system is  $C_{\max} = 1.73$  (Durrani 2010), making it potentially far more efficient than the leapfrog scheme. The modulus of the amplification factor for the RK3 scheme is shown in Fig. 1 as a function of normalized Courant number and normalized wavelength. The damping region with the RK3 scheme is slightly narrower than with the leapfrog scheme, extending from waves of length  $2\Delta x$  to  $12\Delta x$ . The maximum again occurs at  $4\Delta x$  and decreases with decreasing Courant number. Compared with the leapfrog scheme, damping does not protrude as deeply into Courant number space, extending to approximately  $0.5C_{\max}$ .

In addition to investigating the amplitude error, it is useful to examine the difference between the numerical phase speed and actual phase speed of the disturbance (wave). The relative phase ratio is defined as  $r = c_d/c_a$ , where the numerator and denominator are, respectively, the phase speed of the discretized wave and the phase speed of the analytical wave. If the relative phase ratio is less (greater) than unity, then the numerical scheme's solution lags (leads) the analytic solution. For the relative phase ratio of unity, there is no dispersion error. The relative phase ratio is shown in Fig. 2 as a function of the normalized wavelength; data are shown for three values of Courant number: **C1** =  $C_{\max}$ , **C2** =  $C_{\max}/2$ , and **C4** =  $C_{\max}/4$ .

Because of the employed second-order spatial advection operator, the phase speed for both timestepping schemes is zero for the  $2\Delta x$  wave. The leapfrog scheme artificially speeds up the solution for  $4\Delta x$  waves as compared with the analytical wave when using the maximum stable Courant number. This feature is not present in the RK3 time-advection scheme. Figure 2

indicates that there are only minimal differences between the schemes for other values of Courant number. For both schemes, the relative phase ratio becomes very close to unity at  $32\Delta x$ .

### 2.3 Evaluated flow statistics

Evaluated first-order flow statistics included mean virtual potential temperature ( $\bar{\theta}$ ) and means of the horizontal ( $x$  and  $y$ ) components of the flow velocity ( $\bar{u}$  and  $\bar{v}$ , respectively). Among the evaluated second-order statistics are variances of virtual potential temperature ( $\theta'\theta'$ ) and flow velocity components ( $u'u'$ ,  $v'v'$ ,  $w'w'$ ), where  $w$  is the vertical ( $z$ ) component of flow velocity, vertical kinematic heat flux ( $w'\theta'$ ), and horizontal components of the vertical turbulent kinematic momentum flux, ( $\bar{w}'u'$  and  $\bar{w}'v'$ ). Higher-order statistics are represented by the third moments of virtual potential temperature ( $\theta'\theta'\theta'$ ) and the vertical component of flow velocity ( $w'w'w'$ ). The overbars in the above expressions denote the horizontal-plane averages and primes signify deviations from the corresponding averages. The CBL depth (inversion height  $z_i$ ) was evaluated, as in FEA04, by two separate methods: from the height of the maximum virtual potential temperature gradient and from the height of the minimum virtual heat flux.

All the above turbulence statistics were calculated in 200-s intervals. In FEA04, we chose to calculate statistics exclusively through averaging over horizontal planes in order to avoid code comparability uncertainties associated with time averaging. Flow statistics produced by different codes were compared after 10,000 s into the simulation. However, as noted in FEA04, for third-order statistics (as for some second-order statistics), such spatial-only averaging did not provide sufficiently steady estimates due to the limited sample size (equal to the number of grid points in the horizontal plane of the numerical grid). The discrepancies between higher-order statistics were thus found to generally increase with the order of statistics. In order to address and investigate this issue, the simulations in the present study were extended over an additional 30 min to 11,800 s. Complementary to the original time of 10,000 s, profiles of statistics, obtained by plane averaging, were compared at 11,800 s. Additionally, each of the turbulence statistics profiles (computed in 200-s intervals) were averaged over a 30-min period between these two sampling moments, so that the resulting mean profiles could be compared with instantaneous profiles of statistics at the beginning and at the end of the sampling period. Such an averaging approach was intended to evaluate steadiness of the statistics calculated solely by plane averaging. The time-averaging period of 30 min is on the order of the convective overturning time scale (life cycle of a thermal) in the reproduced CBL cases.

The effect of complementary time averaging is illustrated in Fig. 3 for the third-order temperature moment in the GS case. Comparison of statistics obtained by the two averaging methods has shown that an increase of the sample size in the case of the combined spatial and temporal averaging generally leads to smoother profiles of statistics while retaining their essential structural features. In the subsequent plots of statistics to be shown herein, we will present the instantaneous profiles only at 10,000 s along with the 30-min mean profiles (which would be the profiles in a and c panels of Fig. 3). Such a plot layout, on the one hand, allows for a comparison with statistics from FEA04 and, on the other hand, enables tracking of meaningful differences observed in the temporally-averaged statistics retrieved from LES runs with varying Courant number in the RK3 scheme.

One-dimensional spatial spectral densities (spectra) of the resolved  $x$ -direction longitudinal, ( $P_u$ ), and vertical, ( $P_w$ ), velocity components were calculated in  $x$  and  $y$  directions following the method analogous to that described in Kaiser and Fedorovich (1998). These

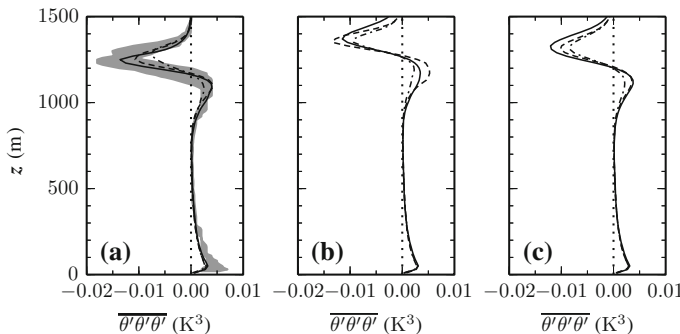


**Fig. 3** Vertical profiles of the third moment of virtual potential temperature for the GS case. **a:** instantaneous profile at 10,000 s; **(b):** instantaneous profile at 11,800 s; **(c):** 30-min mean profile throughout the 10,000 to 11,800 time interval. Solid lines: C1 case; dashed lines: C2 case; and dashed-dotted lines: C4 case. The grey area in **(a)** represents the spread of predictions by different LES codes from [Fedorovich et al. \(2004b\)](#)

spectral calculations were performed at each simulation output time within the last 30 min of simulation and at all 100 vertical levels. The resulting spectrum in the direction of interest ( $x$  or  $y$ ) at a given height was obtained by averaging the individual-row spectra over the corresponding orthogonal direction ( $y$  or  $x$ ) and over the 30-min time interval. For the  $u$  component of velocity,  $x$  is therefore the longitudinal direction with the corresponding wavenumber defined as  $k_1 = 2\pi/\lambda_x$ , and  $y$  is the transverse direction with the wavenumber defined as  $k_2 = 2\pi/\lambda_y$ , where  $\lambda_x$  and  $\lambda_y$  are, respectively, wavelengths along the  $x$  and  $y$  directions. For the  $w$  component of velocity, both horizontal directions and associated wavenumbers are therefore transverse. Based on considerations presented in [Skamarock \(2004\)](#) regarding the utility of spectra for assessing properties of a numerical scheme, velocity spectra allow one to evaluate a code's ability to simulate the spectral distribution of kinetic energy that is consistent with turbulence physics, to quantify effects of numerical schemes on the interactions between simulated turbulent motions of different scales, and to estimate the effective resolution of a simulation. In the present study, spectra are specifically used to gauge the effects of changing the Courant number in the RK3 time-integration scheme on the energy distribution across turbulence scales.

### 3 Results

#### 3.1 NS Case

In this case, the current version of the OU-LES code with the RK3 timestepping scheme yields predictions of the mean features of the CBL vertical structure that are very similar to those reported in FEA04 for the NS case (not shown). The simulated virtual potential temperature profile falls well within the data scatter range from FEA04, although visually the CBL appears to be slightly deeper. Whilst the CBL deepens over the 30-min sampling period, its mean thermal structure remains essentially unchanged, and both mean  $\bar{\theta}$  profiles at 10,000 and 11,800 s are representative of this retained structural similarity. Changing the Courant number value in the RK3 scheme for this case yields no discernible differences between the resulting  $\bar{\theta}$  profiles.

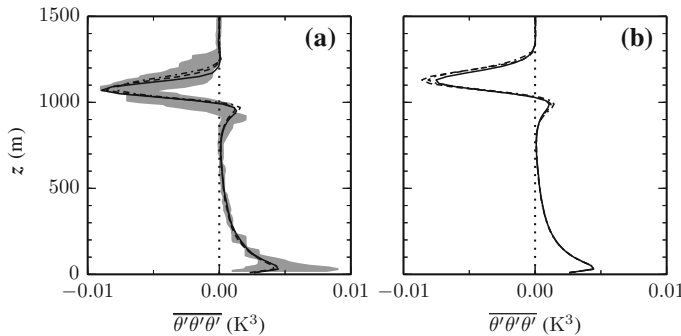


**Fig. 4** Vertical profiles of resolved  $\bar{\theta}'\theta'\theta'$  for the NS case. (a): instantaneous profile at 10,000 s; (b): 30-min mean profile throughout the 10,000 to 11,800 time interval. *Solid lines*: C1 case; *dashed lines*: C2 case; and *dashed-dotted lines*: C4 case. The gray area in (a) represents the spread of predictions by different LES codes from Fedorovich et al. (2004b)

Similarly to first-order statistics, second-order statistics from the conducted simulations fall well within the range of FEA04 values for the considered CBL case (the data are not shown). The lone exception is the  $\bar{\theta}'\theta'$  variance, whose values in the middle of the entrainment zone are slightly larger in the present study than those reported in FEA04. Generally speaking, the behaviour of the second-order turbulence statistics does not appreciably vary over the final 30 min of the simulation. Values of  $\bar{u}'u'$  from the C1 simulation are larger than those from the C2 and C4 simulations throughout the entirety of the CBL, while the opposite is true for the variance of vertical velocity. However, differences between results with varying Courant number are rather minor for all second-order statistics.

Vertical distributions of the third moments of virtual potential temperature and the  $w$  component of velocity also compare quite favorably between the NS case in FEA04 and the reported study. In the case of  $\bar{\theta}'\theta'\theta'$ , newly simulated values are generally within the FEA04 range and only occasionally slightly extend beyond this range. As evident in Fig. 4, the profile of  $\bar{\theta}'\theta'\theta'$  does change between fields at times 10,000 and 11,800 s, mostly throughout the entrainment region in the upper portion of the CBL, where the third moment of temperature experiences a deep minimum. These changes are comparable in magnitude to the changes of  $\bar{\theta}'\theta'\theta'$  profiles between 10,000 and 11,800 s in the GS case shown in Fig. 3. Changing the Courant number causes  $\bar{\theta}'\theta'\theta'$  differences primarily in the entrainment zone. There,  $\bar{\theta}'\theta'\theta'$  values are smaller for the C1 case than for C2 and C4 cases with smaller maximum Courant number values. The same is also true for  $\bar{w}'w'w'$  (the data are not shown).

The evolution of the CBL depth over the entire simulation period was also investigated (results are not shown). With  $z_i$  determined from the level of maximum mean virtual potential temperature gradient (hereafter referred to as the gradient method), the current simulation predicts more rapid growth of the CBL in the first 30 min of the simulation compared to the growth predicted by the model codes that participated in FEA04. A similar faster growth is found with  $z_i$  evaluated from the elevation of minimum kinematic heat flux (hereafter referred to as the flux method), except that it occurs over a shorter period of time and with smaller differences to FEA04. As in FEA04, the gradient-method estimates of  $z_i$  are larger than those from the flux method, which is consistent with previous studies (Sullivan et al. 1998). The depth of the CBL calculated from the gradient method tends towards the high end of the FEA04 data spread, while that from the flux method follows much more closely to the spread centre. Such behaviour is generally congruent with the previously noted

differences between data from this study and FEA04 for the mean profile, variance, and third moment of virtual potential temperature. No major disparities are found between  $z_i$  data from simulations employing different Courant numbers. Also, turbulent velocity spectra calculated from simulations with the three different Courant numbers appear to be quite similar (not shown).

### 3.2 GC Case

Mean profiles of virtual potential temperature and horizontal velocity components for this CBL case compare favorably between FEA04 and the current study. There are also no discernible differences between profiles of either virtual potential temperature or horizontal velocity components at times 10,000 and 11,800 s. Simulations using varying Courant numbers differ only minimally for first-order statistics, with flow fields within the CBL core appearing slightly less mixed in the **C1** case than in both **C2** and **C4** configurations.

As with the first-order statistics, second-order turbulence characteristics from this study are largely in agreement with FEA04. However, within the entrainment zone, vertical profiles of  $\overline{\theta'\theta'}$  and  $\overline{u'u'}$  (Figs. 5 and 6) for the **C1** configuration extend slightly beyond the maxima of the FEA04 range of values. The averaged (over time) profiles of  $\overline{\theta'\theta'}$ , retrieved from the **C2** and **C4** simulations, demonstrate minimal differences in peak values, with the profile maximum from the **C1** simulation occurring at a comparatively lower level. Meanwhile, the peak  $\overline{\theta'\theta'}$  value from the **C1** simulation is larger than the corresponding values from the **C2** and **C4** simulations. Vertical profiles of  $\overline{u'u'}$  from the **C1** simulation point to reduced values of this variance in the mid part of the CBL and a stronger gradient throughout the upper portion of the layer when compared to the counterpart profiles from **C2** and **C4**. The **C1** simulation thus produces notably larger values of the horizontal velocity variance at the CBL top than for the other two simulations with smaller values of the Courant number. Temporally-averaged vertical distributions of  $\overline{w'w'}$  (see Fig. 5) show that the CBL from the **C1** simulation has overall a weaker vertical transport of horizontal momentum than for the **C2** and **C4** simulations. Inhibited vertical transport across the lower portion of the entrainment zone in the simulation with **C1** is a potential reason also for the reduced entrainment heat flux made evident by the  $\overline{w'\theta'}$  profiles shown in Fig. 6. Another notable feature of the CBL structure is the secondary peak in  $\overline{w'w'}$ , prominently visible in Fig. 5. The level and appearance of this secondary maximum, which is shifted slightly upwards compared to the maxima in  $\overline{u'u'}$  and  $\overline{w'\theta'}$ , are consistent with results presented in FEA04. This maximum in the vertical velocity variance close to the upper edge of the entrainment zone (cf. Fig. 6) is a consistently observed feature in LES of the sheared CBL that has not found a physical explanation so far. This apparently points to some unusual mechanism of the turbulence kinetic energy production/redistribution at the very CBL top in the presence of shear.

Vertical profiles of  $\overline{w'w'w'}$  (data not shown) are in good agreement with those reported in FEA04. The current version of the OU-LES code reproduces the slightly negative values of  $\overline{w'w'w'}$  near the surface and in the upper portion of the entrainment zone. These features were previously noted in FEA04. Negativeness of the triple  $w'$  moment close to the ground is apparently a numerical artifact that results from the spatial anisotropy of the numerical grid (Chiel van Heerwaarden, personal communication, 2013). The level of mid-CBL maximum in the  $\overline{w'w'w'}$  profile from the **C1** simulation is slightly lower than in the profiles from other two simulations. On the other hand, the near-surface values of the triple moment from the **C1** simulation are the largest. The negative values of  $\overline{w'w'w'}$  at the CBL top have the largest magnitude in the **C1** case. This feature points to the existence of relatively narrow downward motions that could be associated with the lack of horizontal mixing due to numerical damping

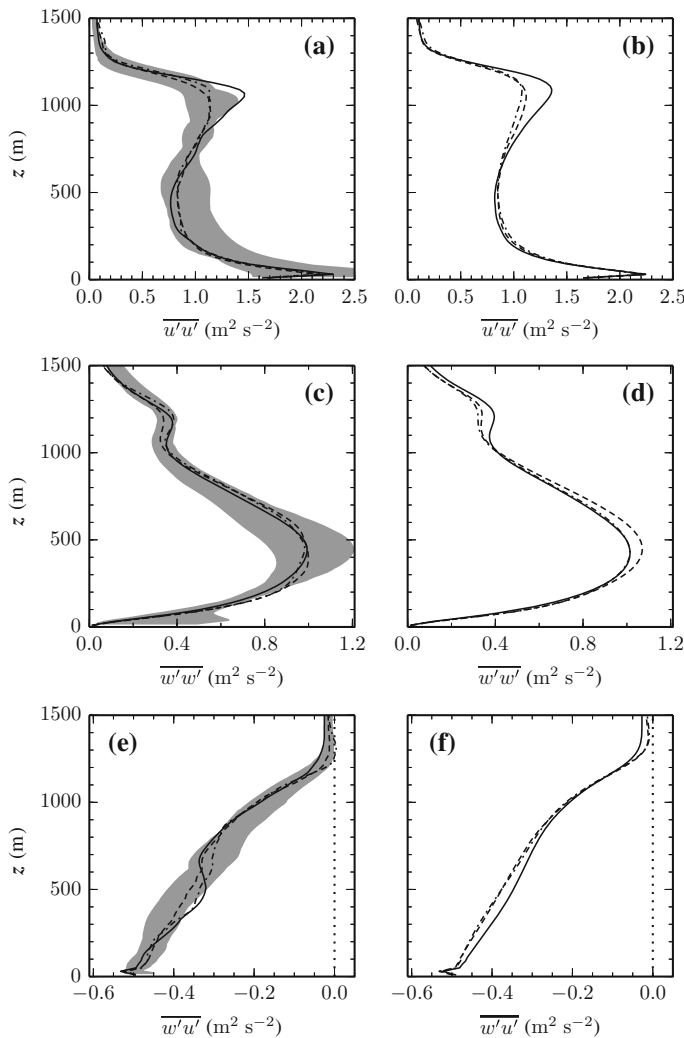


**Fig. 5** Vertical profiles of resolved  $\overline{w'u'}$  (a and b), resolved  $\overline{w'w'}$  (c and d), and total  $\overline{w'u'}$  (e and f) for the GC case. Left panels: instantaneous profile at 10,000 s; right panels: 30-min mean profile throughout the 10,000 to 11,800 time interval. The grey area in the left panels and line styles are as described in Fig. 4

of small-scale turbulence in this case (see discussion of the GC case turbulence spectra below). Vertical profiles of  $\overline{\theta'\theta'\theta'}$  (see Fig. 6) are in reasonable agreement with their FEA04 counterparts, except for those from the C1 simulation that extend beyond the scatter region of the FEA04 data. As noted in FEA04, the positive skewness of  $\overline{\theta'\theta'\theta'}$  in the lower portion of the entrainment zone, combined with the larger magnitude negative skewness in the upper portion of the entrainment zone, is indicative of narrow thermals overshooting their equilibrium level and becoming cooler than the ambient air at the CBL top. The behaviour exhibited in Fig. 6 is associated with rising motions whose thermal intensity and disparity relative to the surrounding environment become more pronounced when the Courant number becomes large. For both considered third-order statistics, differences between individual instantaneous

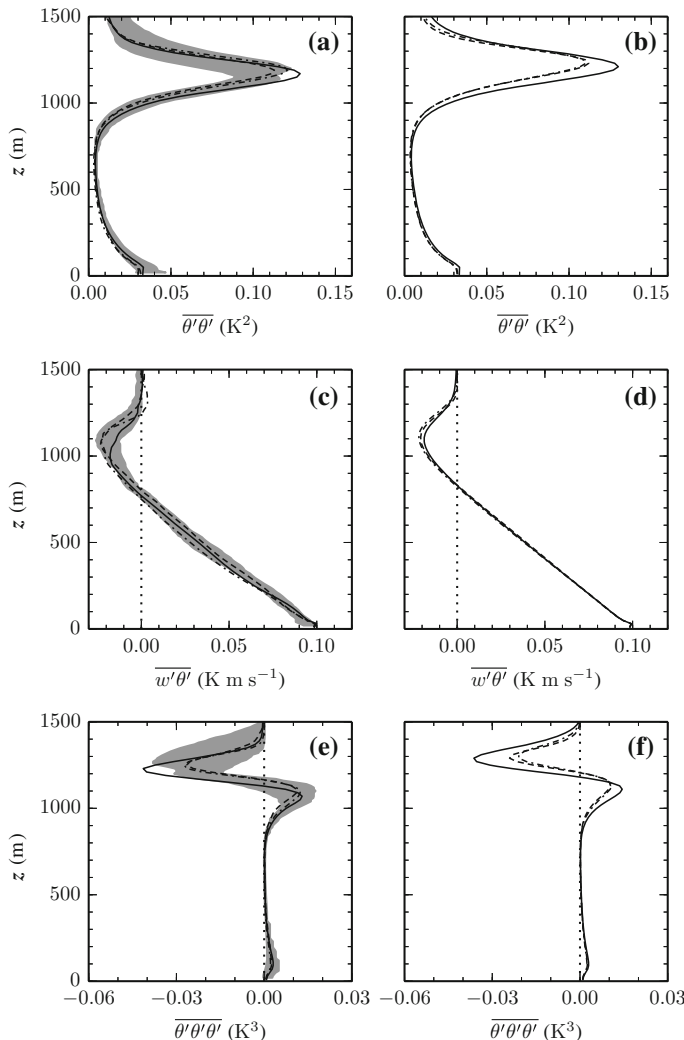


**Fig. 6** Vertical profiles of resolved  $\overline{\theta' \theta'}$  (a and b), total  $\overline{w' \theta'}$  (c and d), and resolved  $\overline{\theta' \theta' \theta'}$  (e and f) for the GC case. Left panels: instantaneous profile at 10,000 s; right panels: 30-min mean profile throughout the 10,000 to 11,800 time interval. The grey area in the left panels and line styles are as described in Fig. 4

values over the final 30 min are quite notable. Such disparities between profiles of the third-order statistics at different times underscore our previously expressed concern, originating from FEA04, regarding the issues with analyzing single (i.e. obtained by plane averaging only) profiles of higher-order turbulence statistics in a sheared CBL.

Estimates of  $z_i$  by the gradient method for this CBL case (not shown) tend toward the high end of the FEA04 range, similar to the  $z_i$  behaviour in the NS case. However, the CBL development in this case does not occur as quickly after the start of the simulation as in the NS case. Values of  $z_i$  reveal a slightly reduced CBL depth in the C1 simulation as compared to that in the C2 and C4 simulations. Estimates for  $z_i$  by the flux method are in the middle of the FEA04 range for the entire simulation and for all Courant number values.

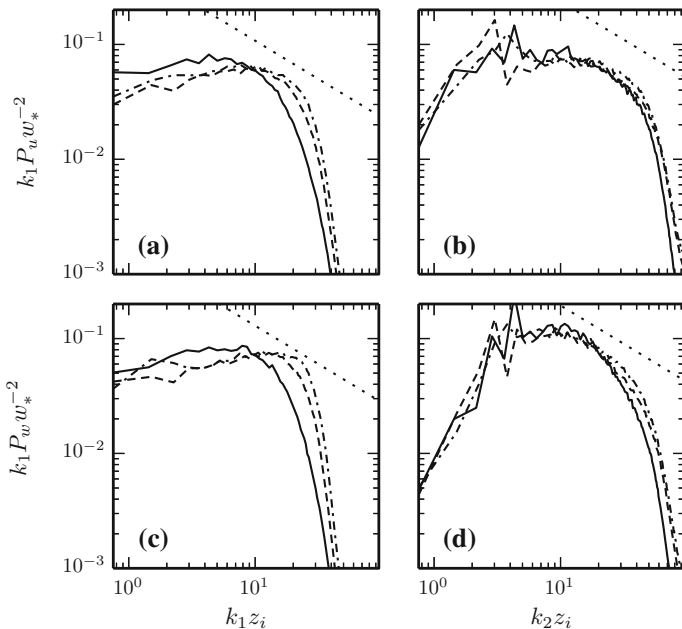


**Fig. 7** Normalized one-dimensional spectral densities (spectra) of the  $u$  (top panels) and  $w$  (bottom panels) velocity fluctuations in the longitudinal ( $k_1$ ; left panels) and transverse ( $k_2$ ; right panels) directions at  $z/z_i = 0.5$  for the GC case. Straight lines indicate  $-2/3$  spectral behaviour expected in the inertial subrange. Line styles are as described in Fig. 4

Spectra of the CBL turbulence were not analyzed in FEA04. They are considered here in order to investigate how changing the Courant number affects scale structure of turbulent velocity fields reproduced with different versions of the RK3 time-integration scheme. Figure 7 shows the one-dimensional normalized spectral densities (spectra) of fluctuations of the  $u$  and  $w$  components of velocity as functions of  $k_1$  (wavenumber in  $x$  direction) and  $k_2$  (wavenumber in  $y$  direction). The demonstrated spectral curves refer to the level of  $z/z_i = 0.5$ , where  $z$  is the height above the ground and  $z_i$  is the CBL depth evaluated via the flux method. This particular height was chosen in order to mask direct effects of the surface on the flow field while remaining within the bulk of the simulated CBL.

A wind-tunnel study by Kaiser and Fedorovich (1998) has shown that wind shear results in a narrowing of the inertial subrange in the velocity spectra and a leveling off the energy production range in the sheared CBL (compared to a shear-free CBL in which energy in the production range decreases with decreasing wavenumber). Velocity spectra retrieved from LES conducted for the GC case with all three tested Courant number values generally confirm these findings regarding shear effects. One may notice, however, that spectra of both velocity components from the **C1** simulation are shifted toward larger scales (smaller wavenumbers) when compared to spectra from the **C2** and **C4** simulations. As may be expected, the magnitude of the shift is largest in the longitudinal (along-flow) spectrum. Turbulence energy is noticeably reduced at large wavenumbers, while its large values are observed at low wavenumbers. Also notable is the substantial decrease in the low wavenumber energy in the  $k_2$  (across-flow) direction for both velocity components as compared to the spectra in the  $k_1$  direction.

For some CBL flow cases considered herein, the visual differences between spectra appear rather insignificant. Note in this respect that the axes in spectral plots are given as a logarithmic scale. Inspection of the fractional differences of the spectral densities between **C1** and **C2/C4** simulations for the **GC** case (not shown) reveal that energy values at smaller wavenumbers in **C1** data are clearly larger. Inspection of smaller scales reveals even more dramatic differences, with **C2** and **C4** simulations generating spectral density values that are as much as 75 % larger than those from **C1**. The **GS** case spectra (discussed later) show smaller differences across the entire wavenumber range.

The discordance of spectral energy values between the  $k_1$  and  $k_2$  directions at low wavenumbers can be examined by inspecting the wavelengths that correspond to the peak values of the smoothed velocity-component spectra. For the  $u$  component of velocity from the **C1** simulation, the wavelength of peak energy is approximately equal to  $4z_i/3$  in the  $k_1$  direction, while the peak of energy in the  $k_2$  direction is at about  $2z_i/3$ . The respective peak energy wavelengths for the  $w$  component of velocity are  $z_i$  and  $z_i/2$ . Physically speaking, this means that CBL turbulent structures with moderate to large wavelengths align primarily in the direction of the mean flow (see Fig. 8), i.e., in the  $x$  direction. As previously noted, the spectrum for both flow components shifts toward low wavenumbers with increasing Courant number. Thus, as the Courant number increases, small-scale flow features are more strongly damped, and the whole spectral structure shifts toward large scales. This effect can be traced visually in Fig. 8. In the velocity patterns from the **C1** simulation, the observed flow structures are relatively broad with minimal spatial variability of velocity components. As the Courant number is reduced, the flow structures become narrower and horizontal variability of the velocity components increases. This visual flow structure exactly matches its spectral structure presented in Fig. 7.

A possible explanation for the spectral shift is found by examining the numerical properties of the RK3 time-integration scheme (see Sect. 2.2). Inspection of the phase and amplification errors of the RK3 scheme makes it clear that the strongest numerical damping in the scheme occurs at the maximum stable Courant number near the  $4\Delta x$  wavelength. The region of prominent damping extends between wavelengths of size  $2\Delta x$  to  $12\Delta x$ . As the Courant number is decreased, the strength and extent of numerical damping are also decreased. It is interesting to note that the damping of small-scale features is substantially stronger in the **GC** CBL than in the **NS** CBL. This difference in behaviour between the two cases is unclear because at a given Courant number the numerical damping (illustrated in Fig. 1) is expected to remain unchanged. It can be shown, however, by calculating the amplification factor for the diffusion part of the employed numerical system, that at larger timesteps the small-scale waves ( $2\Delta x$  to  $4\Delta x$ ) are amplified compared to those at smaller timesteps. Since the **NS** case has a larger timestep for the same Courant number than does the **GC** case, it is possible that energy on the small scales is artificially enhanced due to diffusion in the **NS** case.

The observed spectral behaviour can be related back to the observed features of the second- and third-order statistics. In the **C1** simulation, small-scale energy is damped stronger, leading towards more prominent larger scale flow features and weaker mixing. As a result, convective plumes in this configuration are not properly diffused due to inadequate mixing. This leads to upward motions that are relatively stronger and more disparate from the ambient atmosphere, especially as they surpass their equilibrium level. Additionally, the reduced mixing leads to stronger elevated shear. The result is that the **C1** simulation reproduces larger values of  $\overline{\theta'\theta'\theta'}$  and smaller values of  $\overline{w'\theta'}$  when compared to the other two configurations.

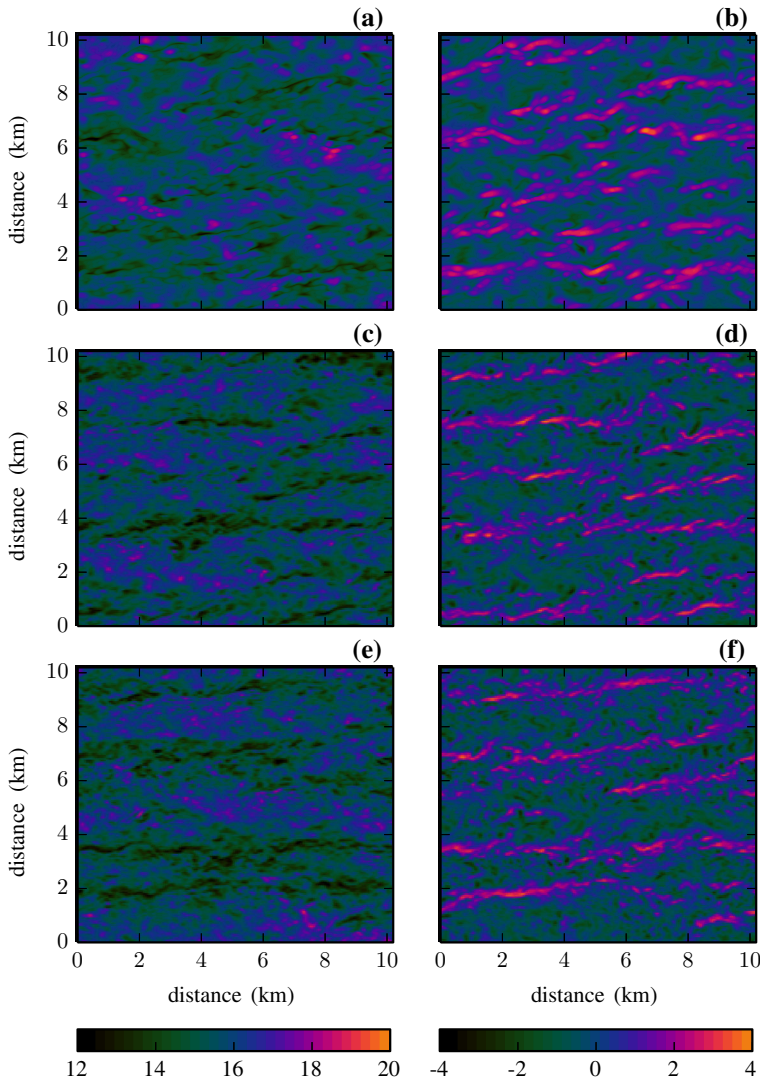


**Fig. 8** Horizontal slices of instantaneous  $u$ -component velocity (left panels) and  $w$ -component velocity (right panels) at level  $z/z_i = 0.5$  during the final hour of the simulation window in the GC case from the **C1** (a and b), **C2** (c and d), and **C4** (e and f) simulations. Colour-scale values are presented in  $\text{m s}^{-1}$

### 3.3 GS Case

Mean profiles of  $\theta$  and horizontal flow velocity components herein match closely with their counterparts from FEA04, analogously to the consistency of mean profiles found for the NS and GC cases. Once again, CBL growth occurs over the final 30 min of the simulation, but principal features of the vertical structure of the layer remain largely unchanged. Differences among mean-flow profiles from the **C1**, **C2**, and **C4** simulations are mostly indistinguishable throughout the CBL. However, the mean  $u$  component of velocity from the **C1** simulation is

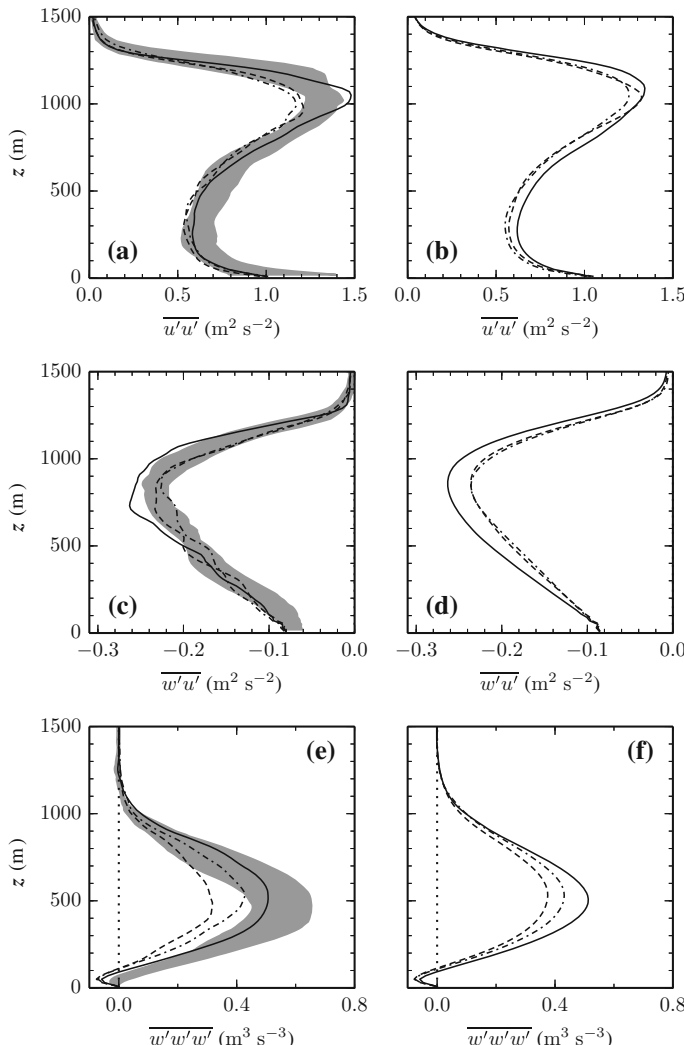


**Fig. 9** Vertical profiles of resolved  $\overline{u'u'}$  (a and b), total  $\overline{w'u'}$  (c and d), and resolved  $\overline{w'w'w'}$  (e and f) for the GS case. Left panels: instantaneous profile at 10,000 s; right panels: 30-min mean profile throughout the 10,000 to 11,800 time interval. The grey area in the left panels and line styles are as described in Fig. 4

slightly more uniform in the vertical (well mixed) than mean  $u$  profiles from the other two simulations, although the differences among all  $u$  profiles with different Courant number are generally smaller in this case than among those in the GC case.

Disparities between second-order statistics are more stark. For  $\overline{\theta'\theta'}$  (the corresponding data are not shown), the C1 simulation yields values within the entrainment zone that are on the upper limit of the reported FEA04 range. Conversely, the entrainment zone peak values of  $\overline{\theta'\theta'}$  from both the C2 and C4 simulations are smaller than those in FEA04. Over the last 30 min of the simulation, the further development of the CBL results in a slightly different alignment of the profiles from the simulations with different Courant numbers.

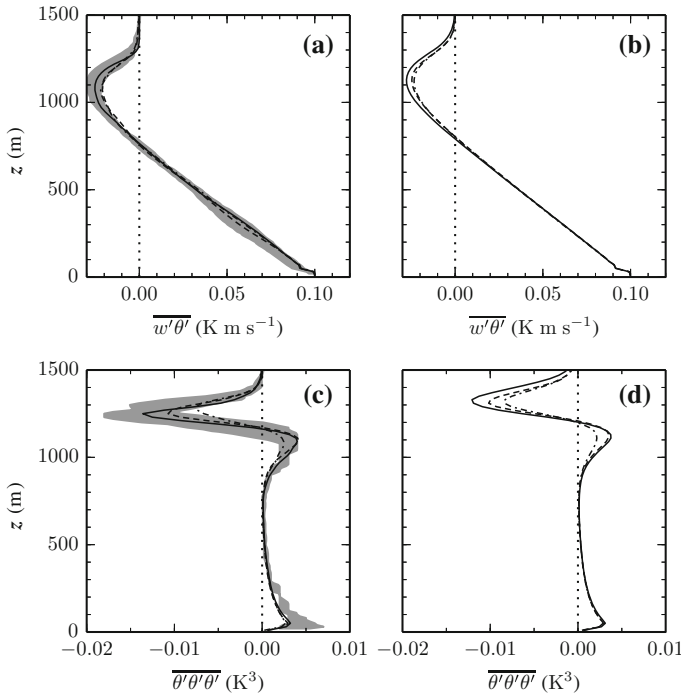


**Fig. 10** Vertical profiles of total  $\overline{w'\theta'}$  (panels **a** and **b**) and resolved  $\overline{\theta'\theta'\theta'}$  (panels **c** and **d**) for the **GS** case. Left panels: instantaneous profile at 10,000 s; right panels: 30-min mean profile throughout the 10,000 to 11,800 time interval. The grey area in the left panels and line styles are as described in Fig. 4

The temporally-averaged profiles of  $\overline{\theta'\theta'}$  show clearer differences between the simulation configurations with different Courant numbers, as compared to their counterparts from the **GC** case. Such a dependence of the temperature variance on the parameters of the numerical integration scheme is only found within the entrainment zone for this case. This is probably to be expected since most turbulence modification by the differently-configured timestepping scheme in this case occurs in the upper portion of the CBL. Similar behaviour is observed in the vertical distributions of the horizontal velocity variance,  $\overline{u'u'}$  (see Fig. 9), with the profile from the **C1** simulation extending beyond the FEA04 extrema and with profiles from the **C2** and **C4** simulations falling on the low side of the FEA04 data scatter. Unlike in the **GC** case, the variance of the  $u$  component of velocity is largest in the **C1** simulation, and decreases with decreasing Courant number throughout the entire CBL depth. The level of peak  $\overline{u'u'}$  in the **C1** simulation is elevated compared with those from the simulations with smaller Courant number.

Profiles of the kinematic momentum flux  $\overline{w'u'}$  (see Fig. 9) from the **GS** case serve as another point of differentiation between turbulence statistics from the **GC** case. The magnitudes of flux values from the **C1** simulation are larger than those reported in FEA04, and are also larger than both the **C2** and **C4** simulations predict throughout most of the CBL depth. Also opposite to the **GC** case, the **C2** and **C4** simulations yield smaller values of  $w'\theta'$  than does the **C1** simulation, as is evident from Fig. 10. The behaviour of  $\overline{w'u'}$  (not shown) is mostly consistent with that reported in FEA04, with the **C1** simulation producing larger vertical velocity variances above the mid-CBL maximum compared to the variance predicted by the **C2** and **C4** simulations.

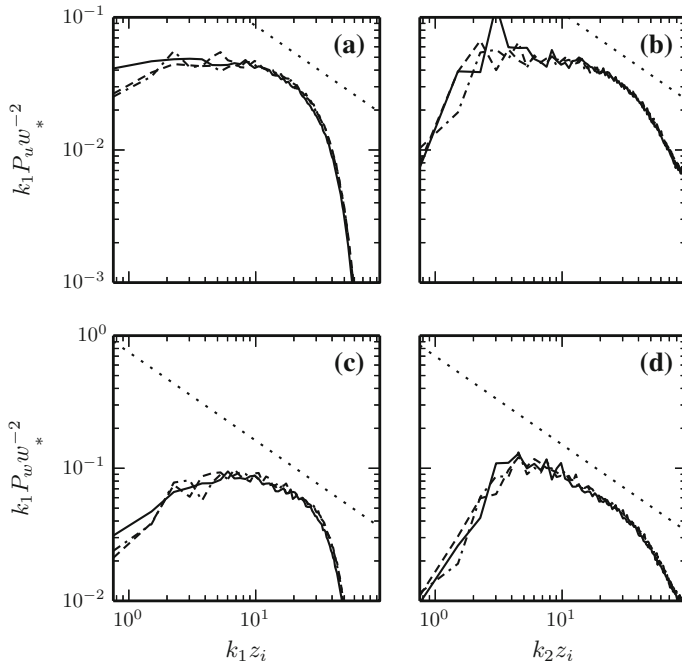


**Fig. 11** As in Fig. 7, but for the **GS** case

As illustrated in Fig. 10, the predicted  $\overline{\theta'\theta'\theta'}$  profiles generally match the corresponding profiles reported in FEA04. The  $\overline{\theta'\theta'\theta'}$  values in the entrainment zone are mostly on the low end of the FEA04 range, especially for the triple moments from the **C2** and **C4** simulations. Compared with the **GC** case, the magnitudes of the considered statistics are smaller. Close to the CBL top, at the upper edge of the entrainment zone, the minimum of  $\overline{\theta'\theta'\theta'}$  deepens with growing Courant number. Profiles of  $w'w'w'$  obtained by plane averaging, see Fig. 9, exhibit a reduced mid-CBL maximum compared with FEA04. Within this region, all profiles but that from the **C4** simulation fall outside of the FEA04 range of values. As in the FEA04 case, the profiles from the present study demonstrate a shallow region of negative  $\overline{w'w'w'}$  near the surface. FEA04 noted that this feature was apparently indicative of numerically reproduced downdrafts in the near-surface layer that are faster than the relatively broader rising motions. The negative  $\overline{w'w'w'}$  values within this region are more pronounced in the profiles herein and extend higher into the CBL than in FEA04. It is hard to say, however, if these features are physically coherent or are just numerical artifacts associated, as in the **GC** case, with numerical grid anisotropy (Chiel van Heerwaarden, personal communication, 2013). In contrast to the two previously discussed CBL cases, the temporally-averaged  $w'w'w'$  profiles retain the same order with changing Courant number as the profiles obtained by plane averaging only: the strongest vertical transport of the  $w'$  variance is found in the **C1** simulation, while the weakest transport is predicted by the **C2** simulation.

Predicted  $z_i$  values for this CBL case (not shown) lie on the high end of the FEA04 range for the gradient used for the  $z_i$  determination method, while those calculated using the flux method are on the middle to low end. The CBL is only slightly deeper in the early portion of the simulation than that in the **GC**-case CBL in FEA04. Predictions of  $z_i$  are generally consistent across both  $z_i$  determination methods and for all three Courant-number values.

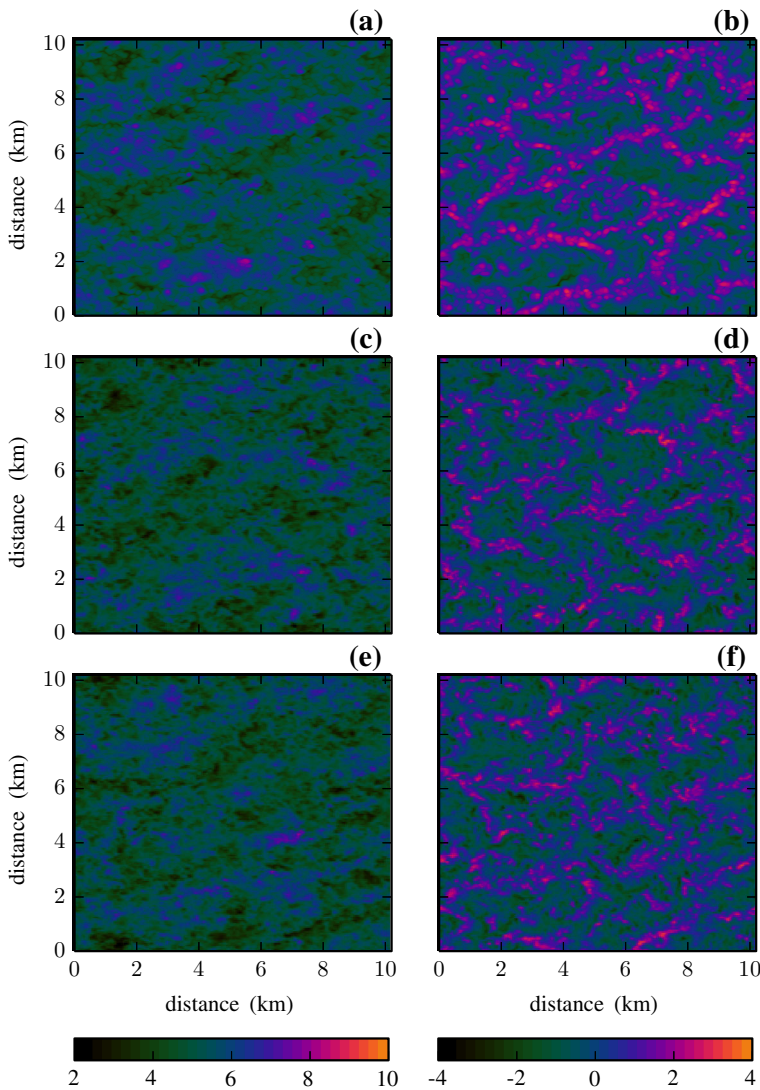


**Fig. 12** As in Fig. 8, but for the GS case

The narrowness of the inertial subranges and the flatness of the energy production ranges associated with the shear influence on turbulence are again present in the velocity-component spectra. However, these spectral features appear reduced in effect, compared with the GC-case spectra, owing to a lower flow speed over the main portion of the CBL, see Fig. 11. In the GS herein, spectral curves from the C1 simulation are only slightly shifted towards large scales along the  $k_1$  direction, and stay in place along the  $k_2$  direction. While the disparities in the longitudinal direction appear visually small, inspection of the fractional differences (not shown) reveal that the spectral densities from the C1 simulation are nearly 25 % smaller at large wavenumbers, and up to 50 % larger at small wavenumbers, as compared to those from the C2 and C4 simulations. The disparity between energy values at low wavenumbers (large

scales) in the  $k_1$  and  $k_2$  directions is still present, although the differences are much more modest than in the **GC** case. This indicates that the CBL large-scale flow structures are not as regularly aligned with the mean flow in the **GS** case as in the **GC** case, or in other words, structures are more evenly oriented along both horizontal directions. Indeed, examination of Fig. 12 indicates that flow structures are more cellular in shape compared with the **GC** case structures. The reduced damping effect of the mean flow velocity on the small-scale turbulent velocity fluctuations is visually identifiable in the horizontal slices of instantaneous velocity-component fields. The resulting spatial variability of velocity clearly increases with decreasing Courant number, although the effects are far less pronounced than in the **GC** case. As noted in FEA04, the flow features in the middle portion of the CBL in the **GS** case are quite similar to the flow features in the **NS** case. The spectra shown in Fig. 11 specifically refer to this flow region. This relates the demonstrated spectra, which feature the reduced numerical damping effects, to the observed cellular structure evident in the vertical velocity field. The overall spectral and structural behaviour of the flow in this case is in line with the previously noted numerical properties of the RK3 scheme.

## 4 Discussion

### 4.1 First-Order Statistics

In terms of the first-order flow statistics (mean flow characteristics), such as mean virtual potential temperature and mean flow components, results from the present study are consistent with flow fields reproduced by various LES codes in FEA04. Predictions from the updated version of the OU-LES code using the RK3 timestepping scheme commonly fall within the scatter of LES predictions from that study. When differences do exist, those are generally small.

### 4.2 Second-Order Statistics

Second-order statistics of fluctuations of the horizontal ( $u$  component) and vertical ( $w$  component) velocity demonstrated sensitivity to both wind shear and properties of the employed time-integration scheme. In the absence of shear (**NS** case), the vertical distributions of  $\overline{u'u'}$  and  $\overline{w'w'}$  compare overall favorably with those from FEA04. This indicates that, in the shear-free CBL, differences in the velocity variances produced using the leapfrog and RK3 schemes are rather small. For this CBL case (**NS**), values of  $\overline{u'u'}$  from the simulation with the largest Courant number (**C1**) are slightly larger throughout the CBL as compared to the variance values from the **C2** and **C4** simulations. Conversely, the **C1** simulation yields smaller values of  $\overline{w'w'}$  throughout the CBL than the corresponding variance values from the **C2** and **C4** simulations. Plainly stated, a reduction in the Courant number yields smaller (larger) horizontal (vertical) velocity-component variances. Since the considered CBL flow regime is dominated by the buoyant production of turbulence that favours vertical flow motion, this motion is expected to be reproduced more realistically with the reduced numerical damping associated with the decrease in the Courant number. The spatial variability of the horizontal flow components, in turn, reduces as the Courant number increases.

In the **GC** and **GS** cases, the variances of the  $u$ -component fluctuations are largest in the regions of strong flow shear near the surface and across the entrainment zone. In both cases, the **C1** simulation produced larger values of the  $u$  variance within these regions than were reported in FEA04. However,  $\overline{u'u'}$  values within the entrainment zone from the **C2**

and **C4** simulations for these cases are smaller than those in FEA04. Throughout the entire CBL, the horizontal velocity variance values predicted for the **GS** case with **C1** are generally larger than the ones retrieved from the **C2** or **C4** simulations. Meanwhile for the **GC** case, the differences between  $\overline{u'u'}$  values from simulations with different Courant numbers are dependent on height. Within the entrainment zone, the **C1** simulation produced larger  $u'$  variances than the ones produced by the **C2** and **C4** simulations. In the middle portion of the CBL, however, the opposite is true. Compared to that in FEA04, vertical profiles of  $\overline{w'w'}$  point to smaller peak values of this turbulence statistic within the CBL. In the presence of shear, the horizontal components of the flow velocity are affected significantly more by variations in the Courant number than in the **NS** case. In the **C1** simulations for both sheared CBL cases, numerical damping in the RK3 scheme considerably affected small-scale flow features. As was revealed by the spectral analyses, the peak spectral energy values in the sheared CBLs are shifted towards small wavenumbers, and energy is relocated to large scales of motion. This explains the enhanced, as compared to that in FEA04, values of the velocity-component variances across the entrainment zones of the sheared CBL. The large wavenumber (small scale) flow features are especially strongly damped in the **GC** case. Such damping results in reduced velocity variability within the CBL as more energy is attributed to larger, on the order of the CBL depth, scales of motion. Accordingly, when the Courant number is reduced, spatial variability of velocity fluctuations within the CBL increases. For the vertical velocity variance in the **GS** case, values from the **C1** simulation are slightly larger than those from both the **C2** and **C4** simulations. Conversely, disparities observed in the vertical distributions of  $\overline{w'w'}$  for the **GC** case are small.

In both sheared CBL cases, profiles of  $\overline{w'u'}$  show a dependence on the vertical distribution of the imposed wind shear and on properties of the employed timestepping scheme. Peak momentum transport occurs just above the surface in the **GC** case, thus it is co-located with the level of the maximum mean shear. In this case, the **C1** simulation yields smaller  $w'u'$  magnitudes throughout the entire CBL in comparison with the **C2** and **C4** simulations. As expected, the level of peak momentum transport in the **GS** case is near the CBL top, again in co-location with the level of the maximum flow shear. In contrast to the **GC** case,  $w'u'$  values in the **GS** case are largest in the **C1** simulation. Interestingly, this reversal between the two sheared CBL cases is also evident in the profiles of kinematic heat flux. While the smaller Courant number values result in larger magnitude  $w'\theta'$  values within the entrainment zone for the **GC** case, the **C1** simulation produces a larger flux in the **GS** case. Such behaviour seems to point to the dependence of simulated turbulence statistics and scale structure of the CBL turbulence on local mean shear effects.

Profiles of  $\overline{\theta'\theta'}$  also show a dependence on the mean flow shear and the time advancement numerics. In the shear-free CBL case, the only appreciable differences between values of this statistic herein and from FEA04 are found in the entrainment zone, where all three versions of the RK3 scheme yield larger  $\theta'$  variance values with the variances from the **C1** simulation being slightly smaller than those from the **C2** and **C4** simulations. It seems likely that the enhanced  $\overline{u'u'}$  values in the **C1** simulation result in limiting the vertical exchange across the entrainment zone. In the sheared CBL cases,  $\overline{\theta'\theta'}$  values from the **C1** simulation are generally greater within the entrainment zone than those reported in FEA04. Behaviour of the temperature fluctuation variance within the entrainment zone differs between the sheared CBL cases for different Courant number values. For the **GS** case, the **C2** and **C4** simulations yield  $\overline{\theta'\theta'}$  values that fall outside of the low end of the corresponding FEA04 range of values, while in the **GC** case the  $\theta'$  variances from the **C2** and **C4** simulations are on the high end of the FEA04 range. In both cases, magnitudes of  $\overline{\theta'\theta'}$  decrease with the reduction of the Courant number. Because in the case of the **C1** simulation more turbulence energy is

attributed to larger scales of motion, as evident from the spectral plots discussed above, the mixing across the inversion, associated primarily with larger turbulence scales (Kaiser and Fedorovich 1998), is apparently stronger.

#### 4.3 Third-Order Statistics

Vertical distributions of  $\overline{\theta'\theta'\theta'}$  in the **NS** case compare favorably with those from FEA04, with the magnitude of the  $\overline{\theta'\theta'\theta'}$  variations throughout the entrainment zone slightly decreasing with the Courant number. For both the **GC** and **GS** cases, the opposite tendency is observed. In the presence of shear, the convective rising motions (thermals) are apparently much larger and more distinct from the ambient atmosphere than in the shear-free CBL case. Smaller scale temperature fluctuations are more aggressively damped with larger Courant numbers in the sheared CBL, as more spectral energy is attributed to larger scales. Because the flow speeds are greatest in the **GC** case, the relative amounts of damping and energy redistribution are also stronger in this case. The combined effect leads to the comparatively large magnitudes of  $\overline{\theta'\theta'\theta'}$  throughout the sheared entrainment zone of the **GC**-case CBL.

As noted in FEA04, the magnitude of  $\overline{w'w'w'}$  is a measure of the vertical turbulent transport of the turbulence kinetic energy (TKE) throughout the CBL. In the **NS** case, large positive values of  $\overline{w'w'w'}$  in the main portion of the CBL are indicative of faster and narrower updrafts relative to the slower and broader descending motions. The magnitude of the upward-directed energy transport in this CBL case is smallest for the **C1** simulation. This, again, is likely due to the over-damping of the small-scale vertical motions by the RK3 numerical scheme. On the other hand, peak positive values of the  $\overline{w'w'w'}$  in the sheared CBL cases are largest for the **C1** simulation. As a result of the relatively large Courant number, the damping of small-scale flow features and redistribution of energy to larger flow structures lead to enhancement of the vertical TKE transport. When the Courant number is reduced, the spectral energy becomes more evenly distributed, and the TKE transport weakens.

#### 4.4 CBL Growth

The evolution of the CBL depth herein follows closely that reported in FEA04. In the **NS** case, the CBL deepens more quickly during the early stages of development than its FEA04 counterpart. The reduced numerical damping of the small-scale features by the RK3 scheme, as compared to the leapfrog scheme, apparently lead to the stronger entrainment, so the CBL develops more rapidly. Differences among  $z_i$  estimates are generally small for all tested Courant number values, except in the **GC** case. There, the **C1** configuration produces a slightly slower developing CBL, which is evident also in second- and third-order turbulence statistics plots.

#### 4.5 Spectral Analysis

Spectral densities of the horizontal ( $u$ ) and vertical ( $w$ ) flow components exhibit a strong sensitivity to the Courant number value prescribed in the RK3 timestepping scheme. In the **NS** case, differences between simulations with different Courant number are expectedly minimal. While the numerical damping of small scales is largest for the **C1** simulation, the amplification and phase errors do not propagate upscale in the low flow speed environment. In the presence of flow shear, the turbulence spectral distributions shift towards larger scales. With the small-scale disturbances being associated with greater local time derivatives than the larger disturbances of the same amplitude and phase speed, the former are damped more

strongly in the simulations. In effect, aliasing effects result in the enhanced low frequency modes under conditions when the large wavenumber features are more aggressively damped. This damping is strongest in the **GC** case, where the flow speeds in the CBL interior are largest. The disparity in the spectral energy distributions at low wavenumbers depend on the directions along which the spectra are calculated. Generally, the large-scale energy is smallest in the  $k_2$  (cross-flow) direction, and the corresponding differences between the along-flow and cross-flow spectra are greatest in the **GC** case. Investigation of the peak energy wavelengths reveals that, in the **GC** case, the flow structures are aligned primarily in the direction of the mean flow. Whilst the low wavenumber differences are also present in the velocity spectra for the **GS** case, they are far more modest. In fact, FEA04 demonstrated that the local nature of the turbulence modification causes the mid-CBL flow structure in the **GS** case to appear more like the structure in the **NS** case. This feature is readily visible in the horizontal slices of vertical velocity (see Figs. 8 and 12), where the flow structures appear mostly cellular in the **GS** case and mostly elongated (roll-like) in the **GC** case. The combined damping and energy redistribution features evident in the spectra are also distinctly visible in the horizontal slices of the  $u$  component of velocity. In both of the sheared CBL cases, the velocity field structures are broader and the velocity patterns show less variability in the **C1** simulations than in the companion simulations with smaller Courant-number values.

## 5 Conclusions

CBL entrainment effects in the presence of imposed wind shear were investigated in FEA04 through comparisons of CBL turbulent flows generated by six state-of-the-art LES codes. One such code, OU-LES, has been updated in recent years through incorporation, among other modifications, of the third-order Runge–Kutta (RK3) time-integration scheme. This study revisited FEA04 by repeating simulations for the three CBL flow configurations from FEA04 using the RK3 scheme. The goal was to assess how CBL turbulence statistics analyzed in FEA04 would be affected by the RK3 scheme with different choice of the Courant number implemented in the scheme.

Results show that, in most cases, data from the conducted simulations with the updated OU-LES code fall within the scatter range of data from different codes that participated in FEA04. When shear is absent (**NS** CBL case), turbulence statistics obtained with the RK3 scheme indicate slightly enhanced entrainment effects compared to FEA04. Conversely, in sheared CBL cases (**GC** with height-constant constant imposed mean wind and **GS** with imposed geostrophic wind speed linearly growing with height), turbulence statistics reveal effects of the RK3 scheme that are essentially location and motion-scale dependent. It is important to note that the employed numerical schemes are non-monotonic. Implications of this property are most apparent in flow regions with strong vertical gradients. This may explain in part why the greatest differences for all considered comparisons occur close to the surface and near the capping inversion.

One of the desired benefits of the RK3 time-integration scheme over the previously Asselin-filtered leapfrog counterpart is the opportunity to use larger timesteps without losing numerical stability and ensuring higher accuracy in time of the obtained numerical solutions. While the RK3 scheme undoubtedly possesses these benefits, results presented show that the choice of Courant number in the RK3 scheme affects evaluated CBL turbulence statistics of different orders. It may also significantly modify turbulence velocity spectra and change the appearance of the simulated flow patterns. Turbulence statistics and spectra resulting from simulations with maximum possible (stability-imposed) Courant number (designated as **C1**

simulations in our study) point to unrealistic energy distribution between different spectral components of motion, mostly skewed toward larger scales. This spectral shift is likely a result of amplitude and phase errors of the timestepping scheme that are enhanced over large timesteps in the presence of strong mean flow. When aiming at the most efficient (with largest possible timestep) CBL-flow computations, reasonable values of first-order statistics (mean flow fields) can be expected, though the higher-order turbulence statistics and spectral characteristics may become substantially modified in this case. These undesirable effects may be strongly reduced when reducing the Courant number to the quarter or even to the half of the stability-determined maximal value (designated as the **C4** and **C2** simulations). Due to the overall efficiency of the RK3 scheme, halving the maximum stable Courant number results in a timestep that is still 15 % larger than the leapfrog scheme's maximum stable value (taking the Asselin-filter constant equal to 0.25), while retaining the beneficial RK3 accuracy. Accordingly, in order to accurately reproduce CBL turbulence statistics, a reduced timestep in the RK3 time-integration scheme should be employed.

**Acknowledgments** The authors wish to thank Alan Shapiro, Louis Wicker, and Lance Leslie for helpful conversations related to the scope of this paper.

## References

- Asselin R (1972) Frequency filter for time integrations. *Mon Weather Rev* 100:487–490
- Deardorff JW (1980) Stratocumulus-capped mixed layers derived from a three-dimensional model. *Boundary-Layer Meteorol* 18:495–527
- Durran DR (2010) Numerical methods for fluid dynamics: with applications to geophysics, 2nd edn. Springer, Berlin, 516 pp
- Fedorovich E, Conzemius R, Mironov D (2004a) Convective entrainment into a shear-free linearly stratified atmosphere: bulk models reevaluated through large eddy simulations. *J Atmos Sci* 61:281–295
- Fedorovich E, Conzemius R, Esau I, Chow FK, Lewellen D, Moeng C-H Pino D, Sullivan P, de Arellano JVG (2004b) Entrainment into sheared convective boundary layers as predicted by different large eddy simulation codes. In: Preprints, 16th symposium on boundary layers and turbulence. Portland, Maine
- Fedorovich E, Nieuwstadt FTM, Kaiser R (2001) Numerical and laboratory study of horizontally evolving convective boundary layer. Part I: transition regimes and development of the mixed layer. *J Atmos Sci* 58:70–86
- Kaiser R, Fedorovich E (1998) Turbulence spectra and dissipation rates in a wind tunnel model of the atmospheric convective boundary layer. *J Atmos Sci* 55:580–594
- Nieuwstadt FTM (1990) Direct and large-eddy simulation of free convection. Proceedings of Ninth International Heat Transfer Conference. Jerusalem, Israel, pp 37–47
- Shapiro A, Fedorovich E (2008) Coriolis effects in homogeneous and inhomogeneous katabatic flows. *Q J R Meteorol Soc* 134:353–370
- Skamarock WC (2004) Evaluating mesoscale NWP models using kinetic energy spectra. *Mon Weather Rev* 132:3019–3032
- Sullivan PP, McWilliams JC, Moeng C-H (1996) A grid nesting method for large-eddy simulation of planetary boundary-layer flows. *Boundary-Layer Meteorol* 80:167–202
- Sullivan PP, Moeng C-H, Stevens B, Lenschow DH, Mayor SD (1998) Structure of the entrainment zone capping the convective atmospheric boundary layer. *J Atmos Sci* 55:3042–3064